Powder Technology 372 (2020) 420–427

Contents lists available at ScienceDirect

Powder Technology

journal homepage: www.elsevier.com/locate/powtec

Three-way coupling of fine particle deposition behavior on a rib-roughened surface

Wenpeng Hong, Yan Liu, Bihui Wang, Haoran Li *

School of Energy and Power Engineering, Northeast Electric Power University, Jilin 132012, People's Republic of China

ARTICLE INFO

Article history:
Received 11 January 2020
Received in revised form 18 April 2020
Accepted 8 June 2020
Available online 10 June 2020

Keywords:
Particle deposition
Rib-roughened surface
Poly-disperse fine particles
Particle concentration
Inlet velocity

ABSTRACT

Fine particles deposition widely exists in natural environment and industrial fields such as air pollution, metallurgy, coal combustion, and geothermal utilization. In this work, the effects of mass concentration of poly-disperse particles and inlet air velocity on particle deposition behaviors in the turbulent flow field were numerically analyzed. Results showed that the particle deposition probability density was not monotonic with the mass concentration. Starting from the third rough structure, the deposition probability density reached a maximum at the mass concentration of 2.78 g/m^3. The non-dimension particles deposition velocity decreased due to the increased velocity, and the reduction was progressively larger. Taking the first rough structure as an example, the particle–structure rebound angle increased by about 10° as the air velocity increased by every 2 m/s. This work helps to clarify the deposition behaviors of fine particulate matter on rough surface, providing support for pipeline cleaning and engineering designs.

1. Introduction

Particulate matter is common in nature and engineering applications [1–4]. Fine particles such as smoke, dust, fog, and haze are suspended in the air, leading to serious environmental pollution, which was regarded as one of the primary culprits of urban environmental pollution [5]. For example, the dust particles from pulverized coal combustion in power plants, automobile exhaust gas, and building smoke emissions have increased in the atmosphere, which severely affects urban air quality and human health. When the particles flow through a wall, the particles will diffuse in the space or deposit on the wall. Researchers have found that arranging transverse ribs in pipes helps to improve the performance of particle removal equipment [6–8]. Actually, the diffusion and deposition behavior of the particles is complicated during the movement. It is difficult to capture the particle deposition behaviors due to the acts of particle–wall collision, rebound and particles agglomeration. Therefore, exploring the deposition behavior of fine particles on rib-roughened surface can not only provide guidance for reducing indoor particle concentration, but can also provide theoretical basis for pipeline cleaning, design, and maintenance.

A large number of experiments and simulations have been previously carried out on particle deposition on a rib-roughened surface. Lai *et al.* [9] and Casarsa and Arts [10] studied particles with sizes of 0.7–7.1 and 0.2–2 μm by experimental study, finding that the deposition velocity of ultrafine particles on rib-roughened surface was approximately identical. In recent years, Barth *et al.* [11] and Casarsa and Arts [12] explored the effect of Reynolds number on the deposition of micron and nano-scale particles. In terms of simulation, Lu and Lu discussed the enhancement of particle deposition on rib-roughened surface under the condition of mono-disperse particles with particle sizes of 1–50 μm together with an air velocity of 5.5 m/s, by changing the height of rib structure [13], arrangement form [14] and shape of the structure [15]. Dritselis [16] and Hemmati and Rafee [17] studied the deposition and distribution of micron (6.7–60 μm) and nano-scale mono-disperse particles on rib-roughened surfaces. Lecrivain et al. [18,19] performed an in-depth study on the deposition characteristics of poly-disperse particles on two-dimensional and three-dimensional rough surfaces respectively. They found that the deposition of particle layers appeared near the rough structure, but the rebound and adhesion between particles and particle–wall were not considered. The results of several studies [20–22] showed the existence of collision, rebound and adhesion between micron-sized particles.

The above studies on particle deposition on a rib-roughened surface were mainly focused on single-size particles. In practice, particle size follows a normal distribution [23]. For the convenience of statistics in experiments, the particle size has to be controlled within a certain range, whereas simulation can implement normal distribution over the entire particle size range, and provide more detailed flow field and particle microcosmic information (the interaction forces of fluid-particle, particle-particle and particle-wall). As mentioned by Yin et al. [24], however, the obvious difference in particle size makes it difficult to determine the mesh size, implying that the movement of small particles cannot be well described. At present, the research on poly-disperse

* Corresponding author.
E-mail address: haoran@neepu.edu.cn (H. Li).

https://doi.org/10.1016/j.powtec.2020.06.021
0032-5910/

particles mainly focused on the generation method [25], particle deposition in porous media [26] and movement on smooth surface [27,28]. However, there are few reports on poly-disperse particle deposition on a rib-roughened surface.

In this paper, the effects of mass concentration of poly-disperse particles and air velocity on deposition characteristics were analyzed. A combination of computational fluid dynamics-discrete element method (CFD–DEM) was employed to investigate the collision, rebounding, and agglomeration between particles as well as particle–wall. The particle deposition behaviors were clarified and the underlying mechanism was explored. This work can provide a deeper understanding and knowledge of the migration and deposition of fine particles in rib-roughened channels, and provide guidance for pipeline cleaning and engineering design of related devices.

2. Dynamic deposition model

The proposed model simulated the movement and deposition of poly-disperse particle in rib-roughened channel. An ANSYS FLUENT CFD method was used to preferentially solve the air-phase flow field. Subsequently, the flow field information was transferred to the DEM software. The flow field data and particle collision information were used to calculate the motion, force, and contact of particle system. Finally, the program was used to update the particle position and motion information before these particle attributes were added to the CFD calculation in the form of momentum, and therefore the coupling of CFD–DEM was realized [29]. The flow chart of the coupled method is shown in Fig. 1. The coupling of the two computing methods was realized through the UDF code in FLUENT and the API interface in EDEM. By selecting the EDEM coupling module in FLUENT, including the coupling methods (Eulerian-Eulerian and Euler-Lagrange methods), coupling area and coupling models (drag and lift models) [30], the two computing methods were connected seamlessly. Note that the approach of describing and analyzing physical phenomena in gas-solid two-phase flow area by combining two or more models have been widely employed [31–33].

2.1. Air–phase model

The fluid in the computational domain was considered incompressible since the flow velocity is low. Considering the anisotropy of turbulence and to obtain more accurate prediction of the flow field information, the Reynolds stress model (RSM) was used to calculate the turbulence field. The governing equations are as follows:

$$\frac{\partial \rho}{\partial t} + \nabla\left(\rho \vec{u}\right) = 0 \tag{1}$$

$$\frac{\partial \rho \vec{u}}{\partial t} + \nabla\cdot\left(\rho \vec{u}\vec{u}\right) = -\nabla p + \nabla\cdot\left(\mu \nabla \vec{u}\right) + \rho \vec{g} - \frac{1}{V}\sum_{i}^{n} \vec{F}_{\mathrm{D}} \tag{2}$$

where ρ is air density, t is time, $\vec{u}$ is air velocity, g is gravitational acceleration, μ is aerodynamic viscosity, V is the volume of a CFD grid element and $\vec{F}_{\mathrm{D}}$ is the drag force, i.e., the dominant force of particle movement and deposition in the rib-roughened channel.

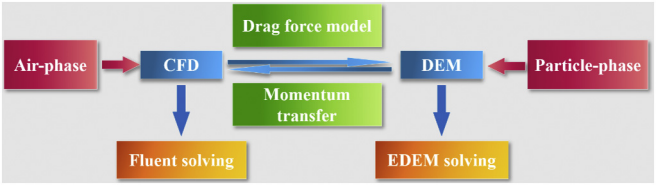

Fig. 1. CFD–DEM coupling process.

2.2. Particle–phase model

The deposition of particles in a rib-roughened channel includes three processes, i.e., movement in flow field, adhesion or rebound with rough surface, and sliding along rough surface. The particle deposition is mainly affected by the contact force (collision and contact adhesion), the non-contact force (non-contact adhesion), the effect of fluid on particles (drag force, Saffman lift force, and buoyancy), and the gravity of particles. A schematic diagram of particle collision, adhesion, and force is shown in Fig. 2. The mathematical model is described as follows:

(1) **Particle motion model**

The Lagrange trajectory tracking method was used to solve the particle motion equation and obtain its trajectory. The particle motion satisfies Newton's second law:

$$\frac{m_{\mathrm{p}} d\vec{u}_{\mathrm{p}}}{dt} = \vec{F}_{\mathrm{G}} + \vec{F}_{\mathrm{ad}} + \vec{F}_{\mathrm{D}} + \vec{F}_{\mathrm{C}} + \vec{F}_{\mathrm{S}} + \vec{F}_{\mathrm{Ar}} \tag{3}$$

where m_{p} is the particle mass, $\vec{u}_{\mathrm{p}}$ is the particle velocity, and the terms on the right side of the equation are gravity, particle adhesion force, drag force, collision, Saffman lift force and Archimedes buoyancy, respectively.

To make the simulation closer to the real situation, the effect of porosity on the resistance of adjacent particles was taken into consideration. For this purpose, the resistance model of DiFelice [34] was employed:

$$\vec{F}_{\mathrm{D}} = \left(0.45 + \frac{3.39}{Re^{0.5}}\right)^{2} \rho A_{\mathrm{p}} \left(\vec{u} - \vec{u}_{\mathrm{p}}\right)\left|\vec{u} - \vec{u}_{\mathrm{p}}\right| \varepsilon^{-(\chi+1)} \tag{4}$$

where Re is Reynolds number; A_{p} is projection area of particles along its radial direction; ε is porosity and $\chi = 3.7 - 0.65 \exp\left[-(1.5 - \lg Re_{\mathrm{p}})^2/2\right]$.

(2) **JKR contact model**

In this paper, Hertz Mindlin with JKR Cohesion [35] contact model, which considered the effect of van der Waals force on the adhesion of particle–particle and particle–wall in the contact area, was employed. The force generated by particle adhesion depends on the overlap, interaction parameters, and surface energy, as shown below:

$$F_{\mathrm{n}} = \frac{4E^*}{3R^*}\alpha^3 - 4\alpha^2\sqrt{\pi\gamma E^*} \tag{5}$$

$$\delta = \frac{\alpha^2}{R^*} - \sqrt{4\pi\gamma\alpha/E^*} \tag{6}$$

$$\frac{1}{E^*} = \frac{1-\upsilon_i^2}{E_i} + \frac{1-\upsilon_j^2}{E_j} \tag{7}$$

$$\frac{1}{R^*} = \frac{1}{R_i} + \frac{1}{R_j} \tag{8}$$

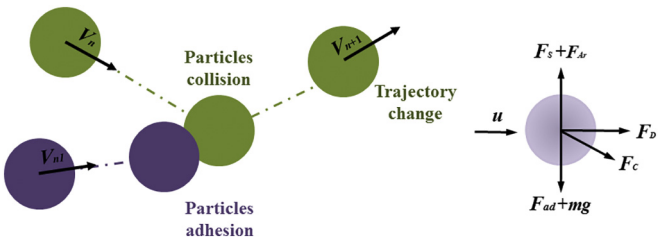

Fig. 2. Schematic diagram of particle collision, adhesion, and force.

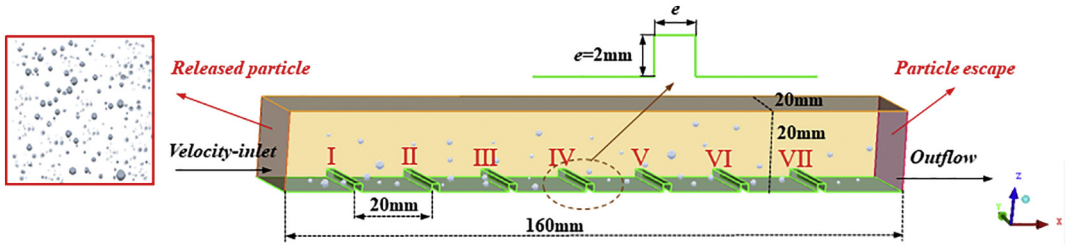

Fig. 3. Computational domain.

where E_i, υ_i, R_i and E_j, υ_j, R_j represent the equivalent Young's modulus, Poisson's ratio, and contact radius, respectively, γ is the surface energy ($\gamma_{p\text{-}p} = 0.01\ J/m^2$, $\gamma_{p\text{-}w} = 0.02\ J/m^2$) [19], and δ is the overlap between particles. The wall was regarded as infinite particles when particles contact with it.

The non-dimensional particle deposition velocity [36] was employed to characterize the deposition of particles, which can be expressed as:

$$V_d^+ = -\frac{hU_0 \ln\left(1 - N_{dep}/N_{in}\right)}{u^* L} \tag{9}$$

where h is the height of the calculation domain, N_{dep} and N_{in} are the total number of particles deposited on the rib-roughened surface and entering the channel, respectively, u^* is the turbulent friction velocity, and L is the length of the calculation domain.

The non-dimensional particle relaxation time [37] based on the time scale of flow is expressed as:

$$\tau_p^+ = \frac{Sd_p^2 u^{*2}}{18\nu^2} C_c \tag{10}$$

where S represents the particle-to-fluid density ratio; C_c is the Cunningham slip coefficient factor, and ν is the aerodynamic viscosity.

3. Simulation conditions

The selected computational region was a rough channel with rib-roughened surface in 3D layout (160 mm × 20 mm × 20 mm), as shown in Fig. 3. In order to reduce the computation cost and time, the boundary function distribution method was employed to initialize the inlet velocity and turbulent kinetic energy. The outflow boundary was used at the outlet. The polydisperse particles (average diameter of 10 μm and size range of 2–50 μm) at 3R (particle radius) were uniformly released from the entrance of the channel. The particle size followed normal distribution [38]. The simulation was finished when all particles were deposited or flowing out of the channel. The main simulation parameters are shown in Table 1.

ICEM software was used to mesh the model as the existence of the rough structure makes the flow field more complex. In order to accurately predict the interaction between particles and the wall, the near-wall mesh was encrypted. The first grid layer was 0.05 mm, y^+ was 1.2, the ratio was 1.2, and a structured mesh was adopted. Considering the influence of computational cost and accuracy, the model with 598,000 meshes was used for calculation after grid independence test.

Table 1
The main parameters used in the simulations.

Parameters	Values	Unit
Particle mean size	10	μm
Ratio of particle-to-air density	2000	–
Air density	1.225	kg/m^3
Restoration coefficient between particle–particle	0.5	–
Restoration coefficient between particle–wall	0.6	–
DEM time step	6×10^{-8}	–
CFD time step	6×10^{-7}	–

4. Verification and validation

It has been reported that the flow field tends to be stable after the fourth rough structure [39]. Therefore, in this paper, the velocity distributions at different positions between the sixth and seventh rough structures were compared with Casarsa's classic experimental results [40], as shown in Fig. 4. The relationship between particle deposition velocity and relaxation time on smooth surface was analyzed, and compared with the experimental [41,42] and numerical [43] results, as shown in Fig. 5. The obtained results are found to be in good agreement with the reported results, indicating that the proposed model is reasonable. In the following sections, the numerical model is used to simulate particle deposition on a rib-roughened surface.

5. Results and discussion

5.1. Turbulent air phase

The flow field has a great influence on the movement of micro-sized particles in channels. In this section, the variation of flow field in rough channel with inlet air velocities ranging from 4 to 8 m/s will be analyzed. The air velocity distributions at 4, 6, and 8 m/s are shown in Fig. 6. It can be seen that with the increase in air velocity, the velocity of the central airflow in the channel is increased significantly, which enhances the carrying effect of small particles and negatively affects particle deposition. The thickness of the boundary layer at the bottom of the channel increases slightly with the change in air velocity. The curves of the thickness at air velocities of 6 and 8 m/s are almost coincided, as shown in Fig. 7. These results illustrate that the thickness of boundary layer is not the dominant factor leading to the change in particle deposition when the air velocity is changed.

Due to the existence of the rough structure, the velocity of airflow on the windward side of the rough structure is suddenly increased. Consequently, the channel on the leeward side of rough structure becomes wider and larger eddy circumfluence appears. Compared with the recirculation zone of the rough structure leeward side after the flow field is stable, it is found that the recirculation zone of the first rough structure leeward side is very large (as shown in Fig. 8). The recirculation zone has a certain lifting effect on the particles, and therefore the turbulent fluctuating velocity perpendicular to the flow direction makes the particles less susceptible to entrainment after flowing through the first rough structure. This results in the larger inertia particles to directly flow through the second rough structure. The eddy recirculation is generated after the flow field is stable, increasing the particle wall-approaching velocity, which is beneficial for particle deposition.

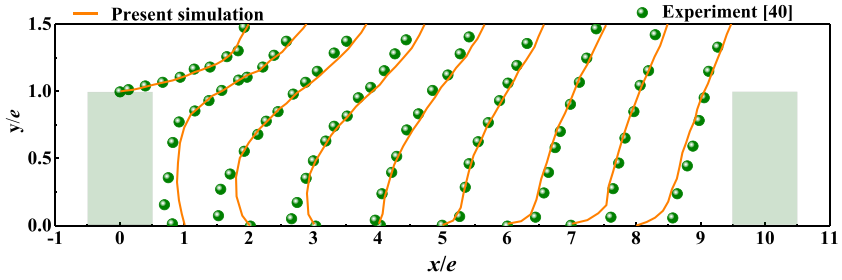

Fig. 4. Airflow velocity between rough structures.

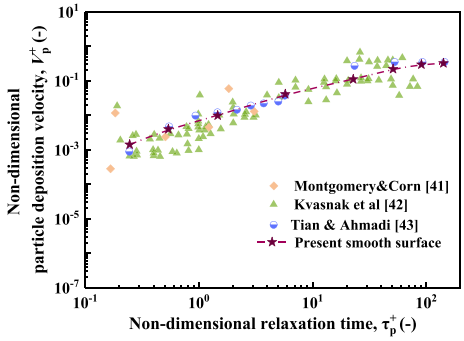

Fig. 5. Non-dimensional particle deposition velocity of smooth surface.

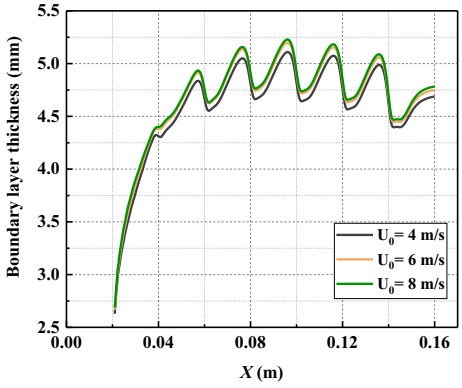

Fig. 7. Variation of boundary layer thickness at different air velocities.

5.2. Effect of mass concentration on particle deposition velocity

It has been reported that the interaction between particles can affect the evolution of the whole system even when the volume fraction of particles is very low [44]. With the increase in particle concentration, the collision, agglomeration, rebound, and adhesion phenomena between particles and wall become more obvious. In this section, the characteristics of particle deposition are studied at different dilute mass concentrations (1.39, 2.09, 2.78, 3.48, 4.17 g/m^3, named C_1–C_5, respectively). The experiment of the particle deposition on rough surface has been investigated by Barth [45], in which the mass concentration of particles was 2.75 g/m^3. To analyze the effect of the particle mass concentration on the deposition behaviors, the value was taken in a small range around the experimental value. Moreover, because the number of particles must be an integer, for convenience, the central mass concentration we selected was 2.78 g/m^3. Note that the particle mass concentration was in dilute phase. The probability density distribution of particles along x direction was analyzed first, as shown in Fig. 9. It is found that the deposition probability density of particles near the first rough structure is the highest, which is not affected by mass concentration. The particles are mainly distributed in the gap between the bottom and the top of the rough structure and are 2.4 mm away from the

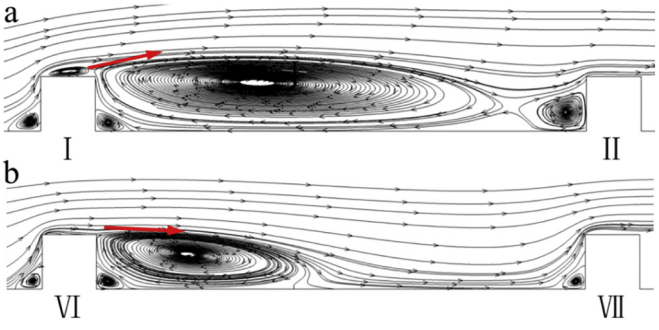

Fig. 8. Recirculation zone downstream of (a) the 1st and (b) the 6th rib.

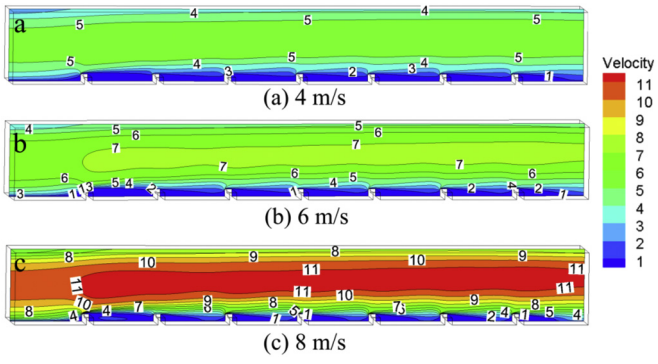

Fig. 6. Distribution of air phase velocity at different inlet velocities (a) 4, (b) 6, and (c) 8 m/s.

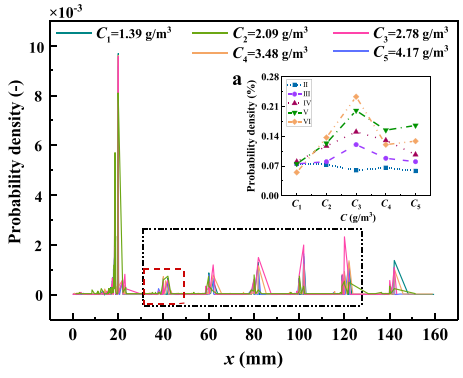

Fig. 9. The probability density distribution along x-direction at different particle concentrations.

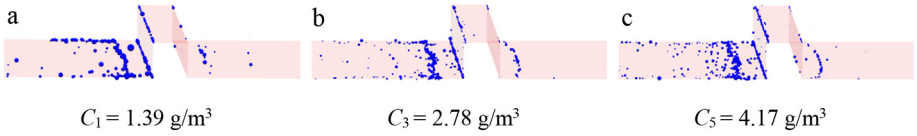

Fig. 10. Distributions of particle deposition near the first rough structure at different concentrations.

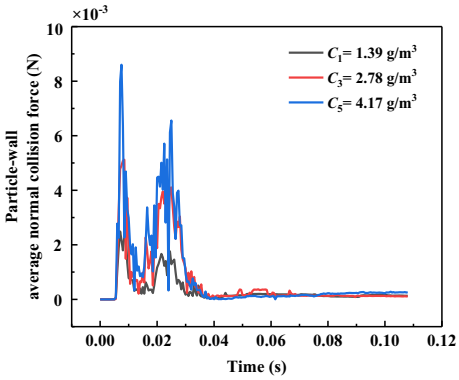

Fig. 11. Time-resolved particle–wall average normal collision force.

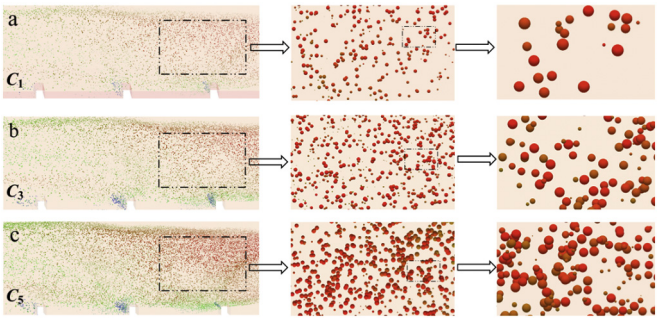

Fig. 13. Particle agglomeration behaviors at different concentrations.

windward side of the rough structure. Moreover, the particles could not deposit easily in the reflux zone due to the influence of small eddy cyclone on the windward side of the rough surface. Finally, they deposited on both sides of the reflux zone. With the increase in mass concentration, a small number of particles are deposited on the windward side of rough structure, and 2 mm away from the leeward side from where the particles are semi-arc distributed, as shown in Fig. 10 (where taking C_1, C_3, and C_5 as examples). Due to the large recirculation region of the first rough structure leeward side, the turbulent fluctuating velocity increases in the direction perpendicular to the flow direction. In addition, the part of the particles that collided with the rough structure are rebounded and raised at a certain angle after bouncing. Therefore, most of the particles flows directly through the second rough structure. Only a few small particles are entrained by the large eddy current, sliding between the two rough elements and finally becoming stationary. Consequently, the probability density of particle deposition near the second rough structure is the smallest, which is about 10% of the first rough structure. The particles are raised at a certain angle and then began to fall, touching the third rough structure. When all rough structures contacting the particles (the simulation time was ~0.02 s), the particle–wall collision is weakened. The average normal collision force (which is defined as the average value of normal force in the duration of single collision and contact) on all particles is shown in Fig. 11. Therefore, from the third rough structure, the probability density of the particle deposition increases gradually until the rough structure in the outlet of the channel, and then it decreases again.

It is found that the probability density of particle deposition of the first two rough structures near the entrance of the channel is barely affected by the mass concentration. From the third rough structure, the probability density of particle deposition reaches the maximum at a mass concentration of 2.78 g/m^3 (as shown in Fig. 9 (a)). It is interesting that the probability density of particle deposition does not increase with the increasing in mass concentration. Firstly, this phenomenon can be analyzed from the aspect of the particle–wall collision degree. From the point of view of the average normal collision force between particles and wall (Fig. 11), the force increases almost in an equal gradient with the increasing in mass concentration. This means that particle–wall collision is not the dominant factor influencing the results. With the increase in particle mass concentration, the contact opportunities between particles are increased. In order to further explore the reasons, the time-resolved average normal collision force and adhesion force between particles are analyzed, as shown in Fig. 12. It is found that the average normal collision force ratio approaches 1:2:8 with the increased mass concentration (Fig. 12 (a)). This result indicates that most of the particles collided with other particles during the movement, which reduced the contact frequency between particles and wall. Moreover, the adhesion force between particles increases greatly when the mass

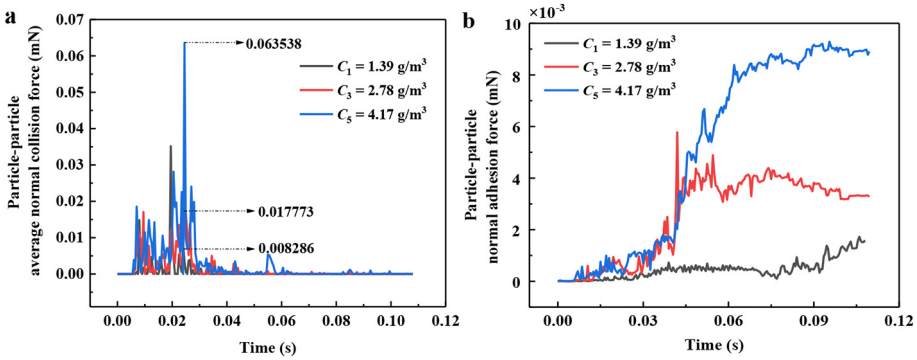

Fig. 12. Time-resolved (a) particle–particle average normal collision force and (b) particle–particle normal adhesion force.

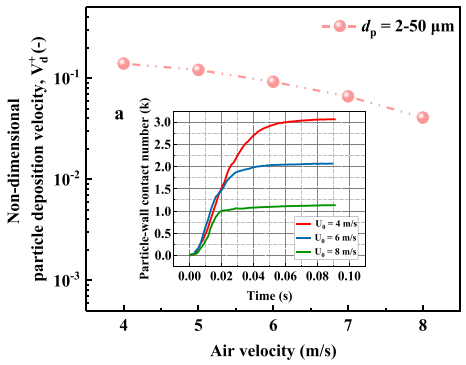

Fig. 14. Particle deposition velocity at different air velocities.

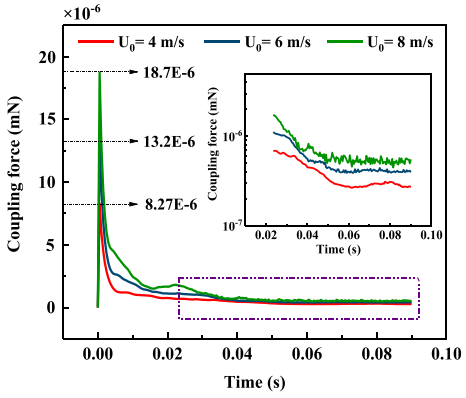

Fig. 15. The force of fluid on particles.

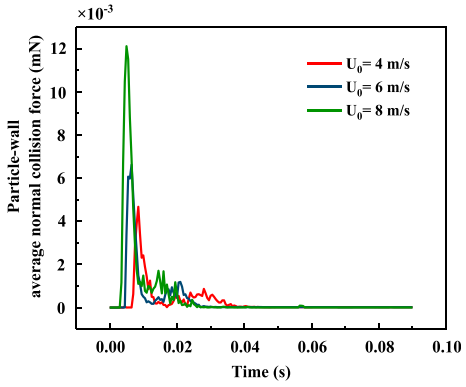

Fig. 16. Particle–wall collision force.

concentration is C_5 (Fig. 12 (b)). Consequently, the particles agglomerate and flow out of the channel during movement. Therefore, when the particle concentration is relatively high, the deposition probability density decreases from the third rough structure. Taking C_1, C_3 and C_5 as examples, the agglomerations of particles during movement are shown in Fig. 13.

5.3. Effect of inlet velocity on particle deposition velocity

The movement of micro-sized particles is closely related to the air flow characteristics in the channel. In this section, the particle deposition in different air velocity channels (4–8 m/s) is simulated, and the effect on particle deposition is explored. The non-dimensional particle deposition velocity under different air velocities is obtained, as shown in Fig. 14. It is found that the non-dimensional particles deposition velocity decreases with the increased air velocity, and the decreased range is progressively larger. In order to further explore the mechanism of particle deposition, the number of particles in contact with the wall was analyzed, as shown in Fig. 14 (a). It is found that when the air velocity is 4 m/s, the particle–wall contact number is higher than that at 8 m/s and lower than that at 6 m/s near the time of 0.02 s. This is because the force of fluid on particles is increased with the increasing in air velocity. The coupling force at 8 m/s is 2.3 times of that at 4 m/s, as shown in Fig. 15. Most of the particles flow out of the channel before touching the wall. When the air velocity is 6 m/s, the entrainment effect of vortices on some small particles overcome the entrainment effect of the main air flow, increasing the contact probability between particles and wall. With the increase in time, the contact number between particles and wall decreases with the increasing in air velocity. The contact number between particles and wall is less than 4 m/s at an air velocity of 6 m/s. At this time, the particles begin to fully interact with the rough structure, and the particle–wall collision force is increased with the increasing in air velocity (Fig. 16). As a result, the particle–wall rebound angle increases (taking the first rough structure as an example, the rebound angle is shown in Fig. 17). The particle–structure rebound angle increases by about 10° as the air velocity increases by every 2 m/s. The rising degree of particles is increased after bouncing, which is because many particles directly flow out of the channel without contacting the following rough structures. Therefore, with the increase in air velocity, the particle deposition velocity is decreased greatly.

In order to further explore the influence of air velocity on particle deposition with different particle sizes, the simulated particle sizes (2–50 μm) are divided into five intervals based on the previous conclusions on the deposition of monodisperse particle on the rough surface, as shown in Fig. 18. It is found that the deposition rate of 30–50 μm particles changes slightly, indicating that the air velocity has little effect on the deposition of relatively larger particles. The deposition rate of the other particles decreases with the increased air velocity, and the deposition rate of 5–20 μm particles decreases greatly. The diameter of 2–5 μm particles increases first and then decreases, and reaches the maximum value at 6 m/s. This is because when the air velocity is 8 m/s, most of the smaller particles flows out of the channel before contacting the wall. While when the air velocity is 6 m/s, the entrainment effect of

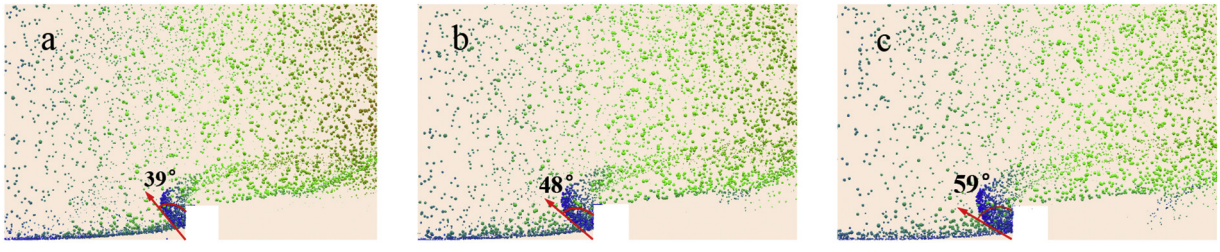

Fig. 17. Variation of particle–rough structure collision angle with air velocities of (a) 4, (b) 6, and (c) 8 m/s.

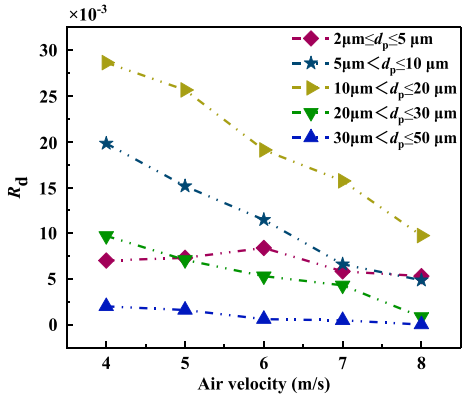

Fig. 18. Deposition rate of particles at different air velocities and size ranges.

vortices on some small particles overcome the entrainment effect of the main air flow, increasing the contact probability between particles and wall.

6. Conclusions

In this paper, the CFD–DEM coupled method was used to simulate the deposition process of polydisperse particles in rough channel with rectangular transverse ribs on the bottom surface. The effects of particle mass concentration and air velocity on particle deposition position and velocity were studied. The following conclusions were obtained:

(1) The air velocity in the center of the channel increased significantly with the increasing in inlet air velocity, which enhanced the carrying effect of small particles. The air velocity had little effect on the thickness variation of the boundary layer at the bottom of the channel. The boundary layer thickness curves at air velocities of 6 and 8 m/s were almost coincided, indicating that the boundary layer thickness was not the dominant factor leading to changes in particle deposition with change in air velocity.
(2) The probability density of deposition of the first two structures at the entrance to the channel was barely affected by the mass concentration of the particles. Starting from the third rough structure, the probability density of particle deposition reached a maximum at a mass concentration of $C_3 = 2.78$ g/m^3.
(3) When the air velocity increased, the coupling force between the fluid and particles increased. The coupling force at an air velocity of 8 m/s was 2.3 times that at 4 m/s, which led to the increase in particle–wall collision force and rebound angle. For every 2 m/s increase in the air velocity, the rebound angle of the particles and the first rough structure increased by about 10°. Therefore, it was observed that the particle deposition velocity decreased with the increasing in air velocity, and the decreased range was progressively larger.

Declaration of Competing Interest

The authors declare that they have no known competing financial interests or personal relationships that could have appeared to influence the work reported in this paper.

Acknowledgement

This work was jointly supported by the National Natural Science Foundation of China (No. 51776032), Planning Project for the "13th Five-Year Plan" on Scientific and Technological Research, the Education Department of Jilin Province (No. JJKH20200106KJ), Science & Technology Development Program of Jilin City (No. 20190104131), and NEEPU Scientific Research Foundation for PhDs (BSJXM-2019102).

References

[1] Y. Qian, Z. Li, L. Yu, X. Wang, X. Lu, Review of the state-of-the-art of particulate matter emissions from modern gasoline fueled engines, Appl. Energy 238 (2019) 1269–1298.
[2] T. Wang, T. Tang, Q. Gao, Z. Yuan, Y. He, Experimental and numerical investigations on the particle behaviours in a bubbling fluidized bed with binary solids, Powder Technol. 362 (2020) 436–449.
[3] T. Tang, T. Wang, Q. Gao, Y. He, Flow and heat mass performances of wet particle drying process based on liquid volume-varying bridge force, Int. J. Heat Mass Transfer 148 (2020) 119037.
[4] H. Li, Z. Yan, Y. Li, W. Hong, Latest development in salt removal from solar-driven interfacial saline water evaporators: advanced strategies and challenges, Water Res. 177 (2020) 115770.
[5] D. Vallero, Air pollutant exposure BT-fundamentals of air pollution, Fundam. Air Pollut 2014, pp. 215–281.
[6] Y. Hemmati, R. Rafee, Effects of the shape and height of artificial 2D roughness elements on deposition of nano and microparticles in the turbulent gas flow inside a horizontal channel, J. Aerosol Sci. 122 (2018) 45–58.
[7] H. Lu, L. Lu, Numerical investigation on particle deposition enhancement in duct air flow by ribbed wall, Build. Environ. 85 (2015) 61–72.
[8] F. Wang, E. Zhang, J. Wang, A study of particle deposition in ventilation ducts with convex or con-cave wall cavity, Procedia Eng. 205 2017, pp. 3285–3292.
[9] A.C.K. Lai, M.A. Byrne, A.J.H. Goddard, Particle deposition in ventilation duct onto three-dimensional roughness elements, Build. Environ. 37 (2002) 939–945.
[10] L. Casarsa, T. Arts, Experimental investigation of the aerothermal performance of a high blockage rib-roughened cooling channel, J. Turbomach. 127 (2005) 580–588.
[11] T. Barth, G. Lecrivain, S.T. Jayaraju, U. Hampel, Particle deposition and resuspension in gas-cooled reactors - activity overview of the two European research projects THINS and ARCHER, Nucl. Eng. Des. 290 (2015) 127–134.
[12] L. Casarsa, T. Arts, Experimental investigation of the aerothermal performance of a high blockage rib-roughened cooling channel, J. Turbomach. 127 (2005) 580–588.
[13] H. Lu, L. Lu, Effects of rib spacing and height on particle deposition in ribbed duct air flows, Build. Environ. 92 (2015) 317–327.
[14] H. Lu, L. Lu, CFD investigation on particle deposition in aligned and staggered ribbed duct air flows, Appl. Therm. Eng. 93 (2016) 697–706.
[15] H. Lu, L. Lu, A numerical study of particle deposition in ribbed duct flow with different rib shapes, Build. Environ. 94 (2015) 43–53.
[16] C.D. Dritselis, Numerical study of particle deposition in a turbulent channel flow with transverse roughness elements on one wall, Int. J. Multiph. Flow. 91 (2017) 1–18.
[17] Y. Hemmati, R. Rafee, Effects of the shape and height of artificial 2D roughness elements on deposition of nano and microparticles in the turbulent gas flow inside a horizontal channel, J. Aerosol Sci. 122 (2018) 45–58.
[18] G. Lecrivain, L. Barry, U. Hampel, Three-dimensional simulation of multilayer particle deposition in an obstructed channel flow, Powder Technol. 258 (2014) 134–143.
[19] G. Lecrivain, D.M. Sevan, B. Thomas, U. Hampel, Numerical simulation of multilayer deposition in an obstructed channel flow, Adv. Powder Technol. 25 (2014) 310–320.
[20] Y. Liu, X. Liu, G. Li, L. Jiang, Numerical prediction effects of particle-particle collisions on gas-particle flows in swirl chamber, Energy Convers. Manage. 52 (2011) 1748–1754.
[21] S. Baghdar Hosseini, R. Haghighi Khoshkhoo, S.M. Javadi Malabad, Experimental and numerical investigation on particle deposition in a compact heat exchanger, Appl. Therm. Eng. 115 (2017) 406–417.
[22] W. Liu, S. Chen, S. Li, Influence of adhesion on random loose packings of binary microparticle mixtures, AIChE J. 63 (2017) 4296–4306.
[23] K. Wang, S. Yu, W. Peng, A novel moment method using the log skew normal distribution for particle coagulation, J. Aerosol Sci. 134 (2019) 95–108.
[24] W. Yin, S. Wang, K. Zhang, Y. He, Investigation of oxygen-enriched biomass gasification with TFM-DEM hybrid model, Chem. Eng. Sci. 211 (2020) 115293.
[25] J. Morán, A. Fuentes, F. Liu, J. Yon, FracVAL: an improved tunable algorithm of cluster–cluster aggregation for generation of fractal structures formed by polydisperse primary particles, Comput. Phys. Commun. 239 (2019) 225–237.
[26] E. Ma, T. Ouahbi, H. Wang, N.D. Ahfir, A. Alem, A. Hammadi, Modeling of the transport and deposition of polydispersed particles: Effects of hydrodynamics and spatio-temporal evolution of the deposition rate, Environ. Pollut. 237 (2018) 1011–1022.
[27] Z. Minhua, D. He, G. Zhongfeng, Computational study of particle packing process and fluid flow inside Polydisperse cylindrical particles fixed beds, Powder Technol. 354 (2019) 19–29.
[28] O.Z. Sharaf, A.N. Al-Khateeb, D.C. Kyritsis, E. Abu-Nada, Four-way coupling of particle-wall and colloidal particle-particle interactions in direct absorption solar collectors, Energy Convers. Manage. 195 (2019) 7–20.
[29] K. Zhang, S. Wang, B. Li, Y. He, Y. Zhao, Heat transfer in a pulsed fluidized bed by using coupled CFD-DEM method, Powder Technol. 367 (2020) 497–505.
[30] S. Wang, W. Yin, Z. Li, X. Yang, K. Zhang, Numerical investigation of chemical looping gasification process using solid fuels for syngas production, Energy Convers. Manage. 173 (2018) 296–302.
[31] B. Peters, M. Baniasadi, M. Baniasadi, X. Besseron, A.E. Donoso, M. Mohseni, G. Pozzetti, XDEM multi-physics and multi-scale simulation technology: review of DEM–CFD coupling, methodology and engineering applications, Particuology 44 (2019) 176–193.

[32] X. Liu, M. Zhao, S. Hu, W. Ge, Three-dimensional CFD simulation of tapered gas-solid risers by coupling the improved EMMS drag, Powder Technol. 352 (2019) 305–313.
[33] K. Zhang, S. Wang, Y. Tang, G. Liu, Y. He, Gas pulsation effect on flow behaviors and heat transfer in a tapered fluidized bed, Powder Technol. 361 (2020) 540–547.
[34] R. Di Felice, The voidage function for fluid-particle interaction systems, Int. J. Multiph. Flow. 20 (1994) 153–159.
[35] K.L. Johnson, K. Kendall, A.D. Roberts, Surface energy and the contact of elastic solids, Proc. R. Soc. A Math. Phys. Eng. Sci. 324 (1971) 301–313.
[36] L. Hongtao, Z. Li, Prediction of particle deposition characteristic in 90° square bend: Square bend particle deposition characteristic, Appl. Therm. Eng. 31 (2011) 3402–3409.
[37] W. Bing, Z. Huiqiang, W. Xilin, Direct numerical simulation of particle deposition, J. Eng. Thermophys. 30 (2009) 90–92.
[38] P.B. Butler, R.G. Schmitt, Shock propagation through a perfect gas entrained with a normal distribution of fine particles, Powder Technol. 63 (1990) 229–240.
[39] M.M. Lohász, P. Rambaud, C. Benocci, Flow features in a fully developed ribbed duct flow as a result of LES, in: Eng, Turbul. Model. Exp. 77 (2005) 59–76.
[40] L. Casarsa, Aerodynamic Performance Investigation of a Fixed Rib-roughened Cooling Passage, Von Karman Institute for Fluid Dynamics, Belgium, 2003.
[41] T.L. Montgomery, M. Corn, Aerosol deposition in a pipe with turbulent airflow, J. Aerosol Sci. 1 (1970) 185–213.
[42] W. Kvasnak, G. Ahmadi, R. Bayer, M. Gaynes, Experimental investigation of dust particle deposition in a turbulent channel flow, J. Aerosol Sci. 24 (1993) 795–815.
[43] L. Tian, G. Ahmadi, Particle deposition in turbulent duct flows-comparisons of different model predictions, J. Aerosol Sci. 38 (2007) 377–397.
[44] F.J. De Souza, A.L. Silva, J. Utzig, Four-way coupled simulations of the gas-particle flow in a diffuser, Powder Technol. 253 (2014) 496–508.
[45] T. Barth, M. Reiche, M. Banowski, M. Oppermann, U. Hampel, Experimental investigation of multilayer particle deposition and resuspension between periodic steps in turbulent flows, J. Aerosol Sci. 64 (2013) 111–124.

Nomenclature

A_P: the projected area of particles in its radial direction (mm^2)
C: particle mass concentration (g/m^3)
C_c: Cunningham slip correction factor (–)
e: height of rough structure (mm)
E^*: equivalent young's modulus (N/m^2)
F_{ad}: adhesion force (N)
F_{Ar}: Archimedes buoyancy (N)
F_C: collision force (N)
F_D: drag force (N)
F_G: gravity (N)
F_S: Saffman lift force (N)
h: the height of channel (mm)
L: the length of channel (mm)
m_p: quality of particle (kg)
N_{dep}: particle deposition numbers to wall (pcs)
N_{in}: incoming particle numbers (pcs)
R^*: equivalent radius (mm)
Re: Reynolds number (–)
S: ratio of particle-to-fluid density (–)
t: simulation time (s)
u: velocity of fluid (m/s)
u^*: frictional velocity of air (m/s)
U_0: average velocity of air (m/s)
u_p: velocity of particle (m/s)
V: volume of unit mesh (mm^3)
V_d^+: non-dimensional particle deposition velocity (–)
y^+: non-dimensional distance from the wall (–)

Greek symbols

α: contact radius (mm)
γ: surface energy (J/m^2)
δ: amount of interparticle overlap (mm)
ε: interparticle porosity (–)
η_{ave}: average relative error (–)
μ: dynamic viscosity of air (Pa·s)
ν: kinetic viscosity of air (m^2/s)
ρ: density of fluid (kg/m^3)
τ_p^+: nondimensional particle relaxation time (–)